AIP | Conference Proceedings

Two-temperature thermodynamic and kinetic properties of transition metals irradiated by femtosecond lasers

N. A. Inogamov, Yu. V. Petrov, V. V. Zhakhovsky, V. A. Khokhlov, B. J. Demaske et al.

Citation: AIP Conf. Proc. **1464**, 593 (2012); doi: 10.1063/1.4739912
View online: http://dx.doi.org/10.1063/1.4739912
View Table of Contents: http://proceedings.aip.org/dbt/dbt.jsp?KEY=APCPCS&Volume=1464&Issue=1
Published by the American Institute of Physics.

Two-temperature thermodynamic and kinetic properties of transition metals irradiated by femtosecond lasers

N.A. Inogamov*, Yu.V. Petrov*, V.V. Zhakhovsky†, V.A. Khokhlov*,
B.J. Demaske†, S.I. Ashitkov**, K.V. Khishchenko**, K.P. Migdal‡,
M.B. Agranat**, S.I. Anisimov*, V.E. Fortov** and I.I. Oleynik†

*Landau Institute for Theoretical Physics, RAS, Chernogolovka 142432, Russia
†Department of Physics, University of South Florida, Tampa, FL 33620, USA
**Joint Institute for High Temperatures, RAS, Moscow 125412, Russia
‡Dukhov All-Russian Science Research Institute of Automatics, Rosatom, Moscow 127055, Russia

Abstract. We consider the thermodynamic and kinetic properties of Nickel as an example of transition metal in two-temperature state $(T_e \gg T_i,)$ produced by femtosecond laser heating. Our physical model includes essential processes induced in metals by ultrafast laser energy absorption. Specifically, the electron-ion collision frequency was obtained from recent high-temperature measurements of electrical conductivity and electron-electron screened Coulomb scattering was calculated by taking into account s-s and s-d collisions. In addition, chemical potential, energy, heat capacity, and pressure were obtained from first-principles density functional theory calculations. This model was implemented in two-temperature hydrodynamic code (2T-HD) and combined with molecular dynamics (MD) to determine strength of molten Ni at high strain rates $\sim 10^8 - 10^9$ s^{-1} under conditions of femtosecond laser ablation experiments. The simulated ablation threshold, which depends on material strength, was found to be in good agreement with our experimental measurements reported here. The combined 2T-HD/MD modeling explains the surprisingly high experimental energy density necessary to initiate ablation in Ni (the experimental crater depth in Ni is several times smaller than in Al and Au, while ablation threshold energies are similar).

1. INTRODUCTION

There are two specific features of ultrashort laser pulses (USLP) which differ them from longer pulses. Those features are: first, appearance of two-temperature (2T) stage when conduction electrons are hot $T_e \gg T_i$ [1–7] and, second, ablation by thermomechanical mechanism when ablated material is mechanically spalled out [3–5, 7, 8]. Contrary to usual spallation from a rear-side boundary in our case spallation takes place at the irradiated frontal boundary [2, 7–10]. Thermomechanical stress should overcome material strength to spall ablated layer [3–5, 7–10]. Therefore there is a sharp ablation threshold on laser absorbed fluence

$$F_{abs}|_{abl.thr} \equiv F_{abl}$$

- there is no thermomechanical ablation below threshold [9]. And therefore amount of ablated material begins from *finite* value $\rho_0 x_{abl}$ when fluence is above threshold

International Symposium on High Power Laser Ablation 2012
AIP Conf. Proc. 1464, 593-608 (2012); doi: 10.1063/1.4739912

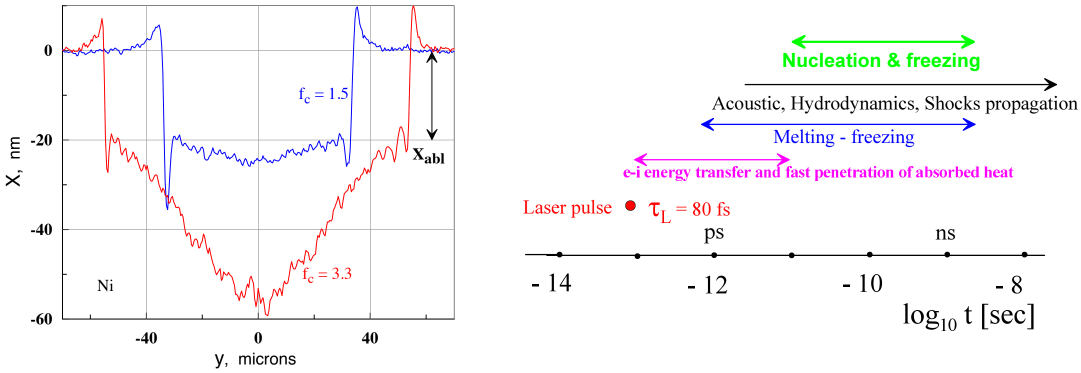

FIGURE 1. (a) (Color online) Crater profiles after USLP impact. The level $x = 0$ corresponds to unperturbed surface. Sharp lateral walls of crater appear in the points where fluence (1.1) achieves the ablation threshold $F_{inc}|_{abl.thr}$. The threshold crater depth x_{abl} (1.3), corresponding to this wall, is marked by the arrow. It is the same for pulses with different central fluence F_c in distribution (1.1). (b) (Color online) Sequence of events: absorption of USLP during τ_L; e-i exchange and fast heat conduction [2]; fast homogeneous melting and slow recrystallization; at acoustic time $t_s = d_T/c_s$ hydrodynamic motion involves depth $\sim d_T$.

$F_{abs} > F_{abl}$ [9], here ρ_0 is density of target material. This amount defines thickness x_{abl} of ablated layer at the threshold, see Fig. 1a.

Final surface profile of Ni target after irradiation by USLP is shown in Fig. 1a. It is obtained by interferometric measurements [11, 12]. Distribution of incident fluence in focal spot is

$$F(y) = F_c \exp(-y^2/R_{las}^2), \quad R_{las} \approx 50 \text{ microns} \tag{1.1}$$

where the y-axis crosses an elliptical (inclined incidence of laser beam) focal spot through its center $y = 0$ along short axis of the ellipse, F_c and $R_{las} \approx 50$ microns are incident fluence at the center and radius of laser beam at a target surface along short axis. Laser beam incident angle is 45^o degrees, p-polarization. In Fig. 1a normalized fluence $f_c = F_c/F_{inc}|_{abl.thr}$ is given. Duration of pulse is 80 fs; wavelength is 1240 nm; near-infrared Chromium-activated Forsterite Cr4+:Mg_2Si0_4 laser is used [13]. Nickel film one micron thick is placed at a glass substrate. Metal surface is irradiated from the air side. In this case the Ni-glass boundary is rear-side of the Ni film.

Ablation threshold is $F_{inc}|_{abl.thr} = 320$ mJ/cm^2. Absorption coefficient as function of incident fluence has been measured. Absorbed fluence at ablation threshold is

$$F_{abl} \approx 140 \text{ mJ/cm}^2. \tag{1.2}$$

Depth of crater at threshold (1.2) is

$$x_{abl} \approx 20 \text{ nm}, \tag{1.3}$$

see Fig. 1a. Crater depth $x_{crat}(F_{abs})$ at $F_{abs} > F_{abl}$ depends on absorbed fluence. There is a rim of positive $x > 0$ residual deformations around lateral wall of a crater.

Sequence of physical processes initiated by USLP is presented in Fig. 1b. Absorption of USLP overheats electron subsystem. Absorbed heat expands from skin layer into bulk by electronic heat conduction. This expansion is rapid during 2T relaxation [2]. During relaxation electron temperature T_e in the heated layer decreases while ion temperature T_i increases in time [1–5, 7]. Depth of the heated layer d_T is established during relaxation stage with duration t_{eq} [2]. Our simulations presented below show that $d_T \approx 60$ nm, $t_{eq} \approx 7$ ps.

The value of the heated depth d_T near threshold fluence (1.2) is important since it defines the crater depth (1.3) and the ablation threshold (1.2). Indeed, simulations show that the depth x_{abl} (1.3) is proportional to the depth d_T. While value F_{abl} (1.2) for fixed material strength is proportional to the depth x_{abl}.

Electron heat conduction coefficient κ is important since it defines the depth d_T. Below our description of coefficient κ for 3d-metal Ni is presented. In one-temperature (1T) case with T_i less than 1 eV the conduction κ is limited by electron-ion (e-i) collisions. In 2T case with high T_e and low T_i the electron-electron (e-e) scattering overcomes the e-i scattering.

In Nickel a d-band is close to Fermi level [6, 14, 15]. In the paper the influence of the d-band on thermodynamic and conductivity κ is analyzed in case of Nickel. Heat flux in Ni is carried by s-electrons mainly. Contribution of the d-band into conductivity κ is small since d-electrons have large effective mass, high collision rate, and low mobility. But the d-electrons are additional scatters for s-electrons transporting energy. The s-s and s-d collision processes, which define e-e conductivity in d-metals, are calculated below. After that the 2T thermodynamics and conductivity results are used to construct model for 2T hydrodynamic simulation. Results of simulations are also presented.

2. TWO-TEMPERATURE THERMODYNAMICS AND EQUATION OF STATE

Dependencies of two-temperature (2T) internal energy $E(\rho, T_e, T_i)$ and pressure $p(\rho, T_e, T_i)$ are necessary to solve 2T-HD equations, because there are heat balances and dynamic equation in the 2T-HD system. DFT calculations were used to find those dependencies. They are shown in Figs. 2 (a,b). The dependencies are well approximated by functions

$$E_e = \left(\frac{\rho}{\rho_0}\right)^{0.6} \frac{KS}{K+S} \; [\frac{\mathrm{J}}{\mathrm{m}^3}], \tag{2.1}$$

$$p_e = 1.1 \left(\frac{\rho}{\rho_0}\right)^{1.1} \frac{KS}{K+S} \; [\mathrm{Pa}], \tag{2.2}$$

where classical (K, Fermi gas limit) and saturated (S) dependencies are

$$K = 1077 \frac{T_e^2}{2} \; [\frac{\mathrm{J}}{\mathrm{m}^3}], \quad S = 1.275 \cdot 10^5 \, T_e^{1.3} \; [\frac{\mathrm{J}}{\mathrm{m}^3}],$$

here electron temperature T_e is in [K]. In Fig. 2a energy E_e is given per unit of mass. Energy density in (2.1) is obtained from values shown in Fig. 2a after multiplication by density ρ. There is a low temperature asymptotic $E_e(\rho_0, T_e, T_i) \approx K$ at $T_e < 10^3$ K.

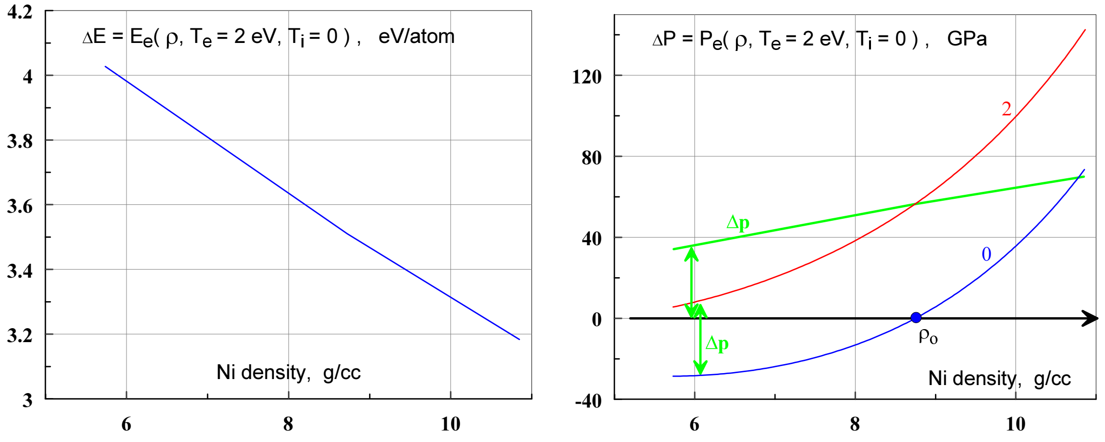

FIGURE 2. (a) (Color online) Electron energy E_e per unit of mass as a function of compression. E_e is a difference between internal energies of the heated $(T_e = 2$ eV) and cold $(T_e = 0)$ Ni crystals. In the case shown here, internal energies have been calculated in the generalized gradient approximation (GGA). (b) (Color online). Total pressure in cold (the blue curve, label "0") and heated up to $T_e = 2$ eV (the red curve, label "2") fcc Ni crystal. GGA. The ions are fixed in their ideal lattice positions $(T_i = 0)$, while temperature T_e is varied. Electron pressure p_e at $T_e = 2$ eV is defined as difference Δp between the heated "2" and the cold "0" curves.

Gruneisen parameter is $\Gamma \approx 1.1(\rho/\rho_0)^{0.5}$. It appreciably deviates from usually supposed value 2/3.

The dependencies shown in Fig. 2 (a,b) are obtained with DFT Abinit [16]. The Monkhorst-Pack mesh of 12^3 mesh points in $\vec{k}$-space covers the Brillouin zone. Results shown in Figs. 2 (a,b) correspond to the generalized gradient approximation (GGA) used for the exchange-correlation functional XC. The GGA gives density ρ_0 and the fcc lattice constant a_0 in equilibrium $p(\rho_0, T_e = 0, T_i = 0) = 0$ equal to $\rho_0 = 4M/a_0^3 =$ 8.73 g/cc and $a_0 = 6.71591$ a.u. = 3.55 Å. Here $M = 58.6934$ is molar mass of Ni isotopes mixture. Density $\rho_0|_{GGA}$ and a lattice spacing $a_0|_{GGA}$ are 2% smaller and 0.6% larger than values 8.902 g/cc, 3.53 Å from reference books for room temperature Ni, respectively. The GGA density $\rho_0 = 8.73$ g/cc is marked by filled circle in Fig. 2b. This is the point where a GGA cold curve intersects the $p = 0$ axis.

Abinit simulation with the local density approximation (LDA) for XC functional gives larger equilibrium density 9.6 g/cc and smaller lattice constant 3.44 Å. Their deviations from reference books are: +7% and -2.5%, respectively. But the deviations of $E_e(\rho, T_e = 2\text{eV}, T_i = 0)$ and $p_e(\rho, T_e = 2\text{eV}, T_i = 0)$ density dependencies of the LDA functions from the GGA functions (the last are shown in Figs. 2a,b) are surprisingly small - of the order of 1%. The same results follows from comparison of E_e, p_e functions calculated with VASP [17, 18] and DMol^3 [19] DFT packages. This stability means that obtained approximations (2.1), (2.2) are reliable. This is significant since for excitations $T_e \sim 2$ eV electron-electron electrostatic energy is not a small value in comparison with the Fermi energy. In this case electron-electron correlations become rather important. Therefore it is not obvious how accurate are the exchange-correlation functionals. Future laser experiments with high resolution may be used to check accuracy of quantum-mechanical simulations.

Let us write two-temperature (2T) internal energy and pressure as sum of two terms

$$E(\rho,T_e,T_i) = E(\rho,T_i,T_i) + [E(\rho,T_e,T_i) - E(\rho,T_i,T_i)], \tag{2.3}$$

$$p(\rho,T_e,T_i) = p(\rho,T_i,T_i) + [p(\rho,T_e,T_i) - p(\rho,T_i,T_i)]. \tag{2.4}$$

The first terms in (2.3), (2.4) refer to one-temperature (1T) state. The second terms

$$E_e(\rho,T_e,T_i) = E(\rho,T_e,T_i) - E(\rho,T_i,T_i) \tag{2.5}$$

$$p_e(\rho,T_e,T_i) = p(\rho,T_e,T_i) - p(\rho,T_i,T_i) \tag{2.6}$$

describe increase of energy and pressure in comparison with their 1T values. This increase is due to excitation of an electron subsystem. We refer to (2.5), (2.6) as electron energy and electron pressure.

We consider conditions when, firstly, at the excited state $T_e \gg T_i$ and, secondly, at all stages (from initial to final) ion temperatures are limited to values

$$T_i \sim 0.3 - 4\,\mathrm{kK} \ll E_F/k_B, \tag{2.7}$$

where E_F is Fermi energy - chemical potential at $T_e = 0$. Under the condition (2.7) the electron contributions to internal energy and pressure are small when system transits to 1T state: $T_e \approx T_i$, since heat capacity of electrons is small in comparison with $3k_B$ at the temperatures (2.7).

At the 2T state (see Fig. 1b) electron energy E_e and pressure p_e are large and important for thermal and momentum balances in a surface layer of an irradiated target. Our approach is based on the assumption that changes in electron energy and pressure $\delta E_e, \delta p_e$ due to changes of T_i in the range (2.7) are small in comparison with values of E_e and p_e at the considered high electronic temperatures (few eV) at the 2T stage and at the fixed mass density. This means that we neglect variations of an integral features of an electron band structure caused by changes in the ion ordering if the density remains unchanged. E.g., electron spectrum of aluminum only slightly deforms during melting [20].

Therefore

$$E_e(\rho,T_e,T_i) \approx E_e(\rho,T_e), \quad p_e(\rho,T_e,T_i) \approx p_e(\rho,T_e). \tag{2.8}$$

Approximation based on this assumption allows to calculate E_e, p_e (2.8) at low ion temperatures. We have calculated the dependency E_e, p_e on T_e and ρ for the case of ideal fcc lattice when $T_i = 0$ as it is written in expressions (2.1) and (2.2) and is shown in Figs. 2 (a,b). Similar approach for tungsten has been described in the paper [21]. Another approach, which includes influence of T_i at the 2T stage, is presented in the paper written by Starikov, Stegailov et al. [22]. The density in our DFT calculations with an ideal lattice is varied through variation of a lattice constant a.

3. ONE-TEMPERATURE EQUATION OF STATE

As was said above, the first terms $E(\rho,T_i,T_i) \equiv E(\rho,T_i)$ in the equations (2.3) and (2.4) are taken from the one-temperature (1T) state. Equations (2.3) and (2.4) describe how to

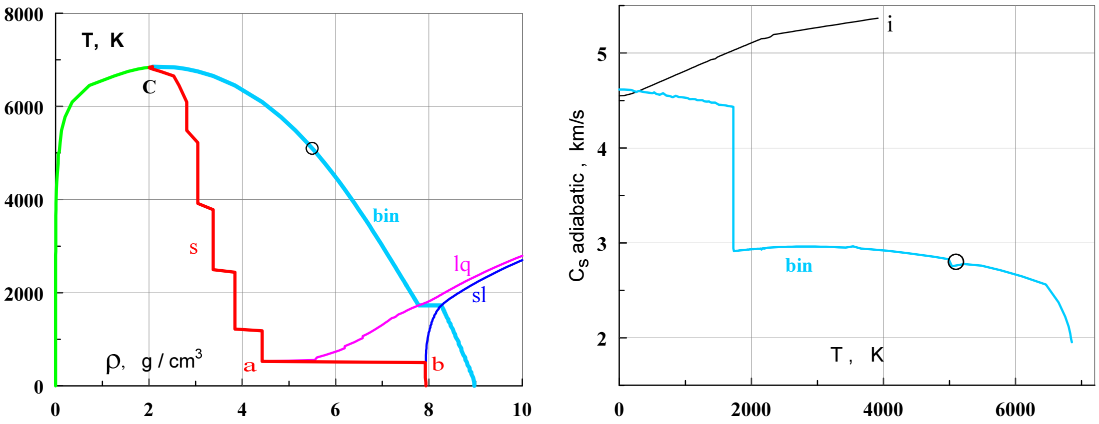

FIGURE 3. (a) (Color online) Phase diagram of 1T Nickel. The binodal curve "bin" divides stable and metastable states. The metastable states are below the "bin". (b) (Color online). Speed of sound $c_s|_s$ in Ni, firstly, at the isochoric curve "i" $\rho = \rho_0$, where ρ_0 is room temperature density, and, secondly, at the curve "bin" shown in Fig. 3a. There are: (1) the jump of c_s at the curve "bin" at the triple point and (2) the change of slope in the point where the isochoric curve "i" intersects the melting curve. The empty circles here and in Fig. 3a define a state with $p \approx 0$ and acoustic impedance $Z = \rho c_s$ equal to Z of room temperature aluminum.

separate electron and ion contributions into the 2T EOS. Wide-range equation of state (EOS) [23] is used in our 2T-HD simulations . Phase diagram of 1T Nickel at ρ, T plane is shown in Fig. 3a. The curve "bin" in Fig. 3a encircles the two-phase vapor-condensed phase region. It has two branches: condensation curve at the left side and sublimation-boiling curve at the right. These branches join together in the critical point "C". The right branch of the curve "bin" consists from three parts. Those parts are: the sublimation curve, the interval of a triple point, and the boiling curve.

Melting region resides as the strip between the upper and lower boundaries. These boundaries are: the solidus "sl" in Fig. 3a and the liquidus "lq". Nickel is in a two-phase solid-liquid mixture state in the melting region. The boundaries limit the melting region from a solid state below and a liquid state above. The melting region at the ρ, T plane in Fig. 3a corresponds to the melting curve at the p, T plane.

Pressure increases along the melting curve together with increasing of density and temperature. Isobaric curves at the ρ, T plane shown in Fig. 3a are horizontal segments inside the melting region.

Let us consider a small piece of material of an irradiated target and its trajectory at the ρ, T plane. The piece changes its density ρ and temperature T during hydrodynamic expansion. These changes define the trajectory of the piece. In the 1T EOS used for 2T-HD simulation a piece of substance does not decay into two-phase mixture with vapor immediately as it intersects the binodal curve "bin" shown in Fig. 3a. The piece below the curve "bin" remains in condensed state. Decay into mixture with vapor takes place when the trajectory achieves the spinodal curve "s". This is scenario of the spinodal decomposition. This scenario approximately describes a picture of decay of stretched substance at high deformation rates $\dot{V}/V \sim 10^9$ s^{-1}. Such rates correspond to our situation with ablation by ultrashort laser pulses.

In our scenario with ultrafast stretching the curves solidus and liquidus continue down inside the metastable region bounded by the binodal curve "bin" in Fig. 3a.

It is important that the curve liquidus "lq" of Nickel intersects the spinodal curve "s" *above* the zero temperature level $T = 0$. The intersection point is marked by the letter "a" in Fig. 3a. This situation is typical for metals. Aluminum is an exception in this sense. In Al the curves "s" and "lq" are separated by finite distance while they decrease down to the level $T = 0$.

There is an equilibrium solid-liquid mixture inside the melting region in the 1T EOS used for hydrodynamic simulation. This assumption holds also below the binodal curve "bin". Existence of the equilibrium solid-liquid mixture becomes impossible below the temperature T_a corresponding to the point "a" of the "s"-"lq" intersection. Therefore at the temperature T_a the spinodal curve "s" undergoes a finite jump to the point "b" shown in Fig. 3a. Further the spinodal "s" follows the curve "sl" below the point "b" during decrease of temperatures.

The position and shape of the spinodal curve "s" shown in Fig. 3a is significant since it defines densities and amplitudes of negative pressures where decay into vapor mixture takes place. At this amplitude the condensed matter ceases to resist to stretching. The phenomenon of decay is dynamically important. Indeed, during decay the pressures change sharply from values of few minus GPa to small values ≈ 0 because at our temperatures vapor pressure is small. Boiling temperature T_{boil} for Ni is 3186 K. Even at this temperature the vapor pressure achieves only dynamically negligible value of 10^{-4} GPa.

4. ELECTRON-ION SCATTERING

It is necessary to have thermal conductivity coefficient $\kappa(\rho, T_e, T_i)$ to run the 2T-HD code. Below the coefficient κ is calculated at $\rho \approx \rho_0$, since fast heat conduction takes place at the approximately isochoric 2T stage. Electron-ion (e-i) collisions dominate above the electron-electron (e-e) processes in contribution to the conduction coefficient κ in most cases. Namely, the e-i processes dominate everywhere on the T_e, T_i plane except the region of cold ions $T_i \sim 300$ K and hot electrons $T_e > 2$ eV. The model of thermal conductivity presented here generalizes the approach [24] developed for single-band metal. New model describes two-band metals with a significant role of the d-band. We consider Nickel as a typical 3d transition metal. Sections 4 and 5 describe electron-ion and electron-electron processes, respectively. Calculations done in Section 5 below include s-s and s-d scattering between electrons from s- and d-bands.

The effective collisional frequency is written as a sum of

$$\nu = \nu_{ei} + \nu_{ee}, \quad \nu_{ei} \approx \nu_{si}, \quad \nu_{ee} \approx \nu_{ss} + \nu_{sd}. \tag{4.1}$$

Transport properties are defined mainly by s-band electrons since they have small effective mass and high mobility. The frequency ν_{si} is defined from the effective Drude relation for electrical conductivity

$$\sigma = n_s e^2 / m_s \nu_{si}, \tag{4.2}$$

where n_s, m_s are concentration and mass of s-electrons, e is electron charge.

Electrical conductivity σ, needed to define the frequency ν_{si}, is taken from published data. The effective e-e frequencies ν_{ss} and ν_{sd} are defined in the next Section from the partial thermal conductivity κ_{ee}. This partial conductivity κ_{ee} includes only the e-e scattering. The conductivity κ_{ee} is calculated in the next Section from the solution of kinetic equation in the $\tau-$approximation by using the scattering matrix for the screened Coulomb interaction between electrons.

In this Section we consider the e-i processes. The effective frequency ν_{si} is obtained from equation (4.2). After that we put it and the e-e frequencies (from the next Section) into equation (4.1), and finally receive κ for 2T Nickel using Drude relation for thermal conduction

$$\kappa = (1/3)\, C_s u_s^2/\nu. \tag{4.3}$$

In (4.3) C_s is an electron heat capacity of s-electrons per unit volume,

$$u_s^2 = (1.3 + 0.4 \cdot 10^{-4} T_e) \cdot 10^{16} \ [\mathrm{cm}^2/\mathrm{s}^2]$$

is an averaged square of s-electron velocities, T_e is in [K].

The total energy E_e (2.1) and the total electron heat capacity C are used in the electron heat balance equation for description of energy E_e of an electron subsystem and its time derivative. Expression for the total heat capacity C is obtained from differentiation of electron energy E_e (2.1) by the temperature T_e at fixed volume V.

But to find diffusive electron heat flux, partial heat capacity C_s of the s-band electrons is necessary, since main contribution into conductive thermal energy transport is connected with s-electrons. We approximate by two parabolas the density of state (DOS) of electron spectrum to find partial heat capacity C_s. One parabola corresponds to s-electrons, and the second parabola corresponds to d-electrons. Calculations show that at electron temperatures $T_e \sim 2$ eV and higher the s-electrons dominate in heat capacity. What was said above about the partial heat capacity C_s in the coefficient of heat conduction refers to all three scattering processes: (1) s-electron collisions with ions s-i, effective frequency is ν_{si}; (2) s-s collisions, ν_{ss}; and (3) s-d collisions, ν_{sd}.

Fig. 4 (a,b) presents 1T dependencies of $\sigma_{ei} \approx \sigma_{si}$ and effective frequency ν_{si} on temperature T for the case $T_e = T_i = T$. We suppose that in 2T case the frequency of collisions of s-electrons with ions per one s-electron $\nu_{si}(T_e, T_i) \approx \nu_{si}(T_i)$ weakly depends on electron temperature T_e, since an amplitude of scattering of s-band electrons on ions is mainly defined by ion ordering. Therefore dependence of κ_{si} on T_e is connected with reduction of degeneracy degree and increase of s-band heat capacity C_s with increase of T_e.

5. ELECTRON-ELECTRON SCATTERING

Band structure of Nickel is shown in Fig. 5a. This structure is approximated by s- and d-parabolas. Density of state per atom in these bands can be written as

$$g_s = \frac{\sqrt{2}}{\pi^2} \frac{m_s^{3/2}}{n_{at} \hbar^3} \sqrt{\varepsilon - \varepsilon_s}, \quad g_d = \frac{\sqrt{2}}{\pi^2} \frac{m_d^{3/2}}{n_{at} \hbar^3} \sqrt{\varepsilon - \varepsilon_1}, \tag{5.1}$$

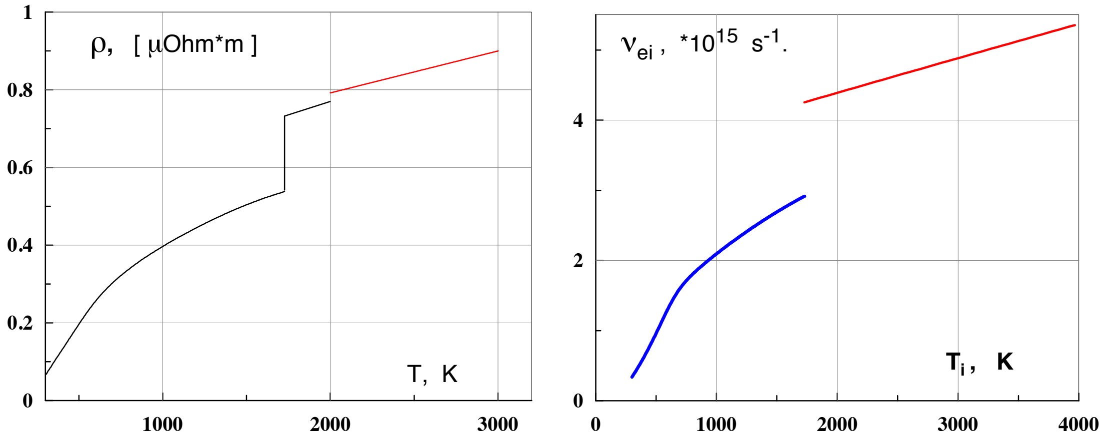

FIGURE 4. (a) (Color online) Experimental dependencies of 1T static electrical conductivity in solid and liquid Ni from [25, 26]. (b) (Color online) Collision frequency obtained from data for σ and equation (4.2).

with electron effective masses

$$m_s = \frac{(3\pi^2)^{2/3}}{2} \frac{\hbar^2 [n_{at} N_s(T_e = 0)]^{2/3}}{e_s}, \quad m_d = \frac{(3\pi^2)^{2/3}}{2} \frac{\hbar^2 [n_{at} N_d(T_e = 0)]^{2/3}}{e_1}. \tag{5.2}$$

Corresponding dispersion laws are

$$\varepsilon(\mathbf{p}) = \varepsilon_s + \mathbf{p}^2/2m_s, \quad \varepsilon'(\mathbf{p}') = \varepsilon_1 + \mathbf{p}'^2/2m_d. \tag{5.3}$$

The approximation (5.1,5.2) allows to divide partial contributions of s- and d-electrons. We calculate s-band heat capacity C_s using the two-parabolic approximation.

In (5.1,5.2) $n_{at} \approx 9 \cdot 10^{22}$ cm^{-3} is concentration of Nickel atoms at normal conditions. The parameters describing s- and d-parabolas in Fig. 5a are: $\varepsilon_s = (-8.6) - (-8.8)$ eV, $\varepsilon_1 = (-4) - (-4.5)$ eV, $\varepsilon_2 = 0.17 - 0.2$ eV. Energy ε in Fig. 5a is measured from zero temperature chemical potential $\mu(T_e = 0)$ (Fermi energy). Nickel is metal with variable number 1-2 of the valence electrons. We suppose that there are $N_s(T_e = 0) = 1.5$ in s-band at low temperatures. Variation of $N_s(T_e = 0)$ in the range from 1 to 2 slightly influences results. Total number of electrons from 3d- and 4s-bands are: $N_s + N_d = 10$. Effective masses are: $m_s = 1 - 1.2$ and $m_d = 6.8 - 7.7$ in units of vacuum electron mass m_e.

Parabolic approximation (5.1,5.2) is necessary to calculate s-s and s-d scattering and the 2T heat conductivity, since in our calculations presented below the s- and d-electrons are considered as free moving particles with dispersion laws (5.3). They interact via screened Coulomb potential. Results of calculations are shown in Fig. 5b. The final value is the effective frequency ν_{se} of the s-e collisions. This frequency is added to the ν_{si} frequency of the s-i collisions, see equation (4.1). After that we obtain the required quantity - the 2T heat conduction coefficient $\kappa(T_e, T_i)$ using equation (4.3).

Calculation of the frequency ν_{es} includes three steps. At the first step we evaluate the frequencies $\nu_{ss}(\mathbf{p})$ and $\nu_{sd}(\mathbf{p})$ as functions of momentum $\mathbf{p}$ of s-electron. The function $\nu_{ss}(\mathbf{p})$ has been found in paper [24]. Cumbersome procedures are required to

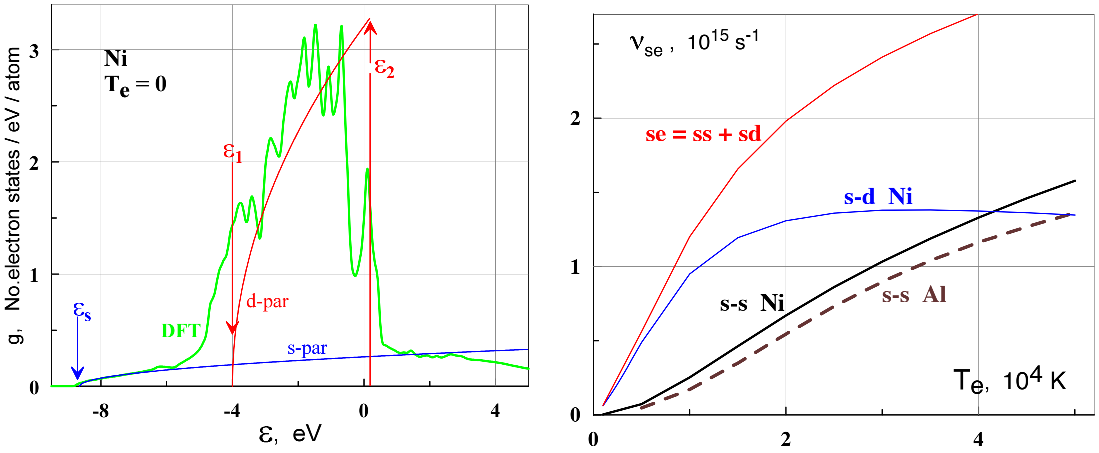

FIGURE 5. (a) (Color online) The "DFT" curve presents the Ni s- and b-bands according to DMol^3 [19] in simulation with all 28 electrons included. The DFT electron spectrum is approximated by two parabolas for s- (s-par) and d-bands (d-par). The arrow ε_s marks the bottom edge of s-band. The arrows ε_1 and ε_2 limit the d-band. (b) (Color online) Electron-electron collision frequencies for ss scattering in Al and Ni, for sd scattering in Ni, and total frequency ν_{se} of collisions of s-electron with s- and d-electrons "se=ss+sd". Compare the frequency $\nu_{se}(T_e)$ with frequency $\nu_{si}(T_i)$ plotted in Fig. 4b.

find function $\nu_{sd}(\mathbf{p})$. They are much longer than in the case of s-s scattering considered before [24], since now we have two different particles with different dispersion laws (5.3). Main technical complication follows from the fact that the d-band has the upper edge e_2 which bounds the parabolic law (5.3), see Fig. 5a. We have to analyze a six-dimensional integral to find the function $\nu_{sd}(\mathbf{p})$.

At the second step we put the function $\nu_{sd}(\mathbf{p})$ into expression for coefficient κ_{sd}. This expression follows from kinetic equation in $\tau-$approximation, where $\tau = 1/\nu_{sd}(\mathbf{p})$. At the simple third step we define the average s-d collisional frequency $\bar{\nu}_{sd}$ from Drude equation (4.3) and the coefficient κ_{sd} defined at the second step. Finally, as was said, we obtain the sum $\bar{\nu}_{sd} + \bar{\nu}_{ss} + \nu_{si}$ (4.1) and put it into equation (4.3).

We describe here the s-d processes, since the s-s scattering has been presented before [24]. Consider the collision of s-electron having the momentum $\mathbf{p}$ with the d-electron having momentum $\mathbf{p}\prime$

$$\mathbf{p} + \mathbf{p}\prime \longrightarrow (\mathbf{p} + \mathbf{q}) + (\mathbf{p}\prime - \mathbf{q})$$

Here $\mathbf{q}$ is a transferred momentum. Then the frequency of collisions of s-electron with the momentum $\mathbf{p}$ with d-electrons can be written as

$$\nu_{sd}(\mathbf{p}) = \frac{2\pi}{\hbar} \int \frac{u^2(q)\, d^3q}{(2\pi\hbar)^3} \int \frac{2d^3p\prime}{(2\pi\hbar)^3} S(\mathbf{p}, \mathbf{p}\prime, \mathbf{q})\, \delta[\varepsilon(\mathbf{p}) + \varepsilon\prime(\mathbf{p}\prime) - \varepsilon(\mathbf{p} + \mathbf{q}) - \varepsilon\prime(\mathbf{p}\prime - \mathbf{q})]$$

The interaction between electrons is described by the screened Coulomb potential

$$U(r) = \frac{e^2}{r} e^{-\kappa r}, \quad u(q) = \frac{4\pi e^2}{\kappa^2 + q^2/\hbar^2}$$

with the screening length $\lambda = 1/\kappa$ (not to be confused with heat conductivity).

Statistical factor

$$S(\mathbf{p},\mathbf{p}\prime,\mathbf{q}) = f_d(\mathbf{p}\prime)[1-f_s(\mathbf{p}+\mathbf{q})][1-f_d(\mathbf{p}\prime-\mathbf{q})] + f_s(\mathbf{p}+\mathbf{q})f_d(\mathbf{p}\prime-\mathbf{q})[1-f_d(\mathbf{p}\prime)]$$

is defined by the electron s- and d- energy bands, here $f = 1/(1+\exp((\varepsilon-\mu)/T_e))$ is Fermi distribution function for s- (f_s) and d- (f_d) electrons. We use energy conservation in s-d collision to simplify the factor S. After that integrations over azimuthal and polar angles in the $\mathbf{p}'$ and $\mathbf{q}$ spaces have been performed. This allow us to reduce the multiplicity of integration in expression for $\nu_{sd}(\mathbf{p})$ from six dimensions to two dimensions over the plane p', q. Making these last integrations $dp'\,dq$ we obtain the required dependence $\nu_{sd}(\mathbf{p})$. This is the end of the first step from the sequence of the above described three steps.

At the second step, from the obtained dependence $\nu_{sd}(\mathbf{p})$ we define the thermal conductivity coefficient due to s-d electron scattering

$$\kappa_{sd}(T_e) = \frac{k}{3}\int(\varepsilon-\mu)\left(-\frac{\partial f_s(\varepsilon)}{\partial\varepsilon}\right)\left(\frac{\partial\mu}{\partial T_e}+\frac{\varepsilon-\mu}{T_e}\right)\frac{v_s^2(p)}{\nu_{sd}(p)}\frac{p^2dp}{\pi^2\hbar^3}, \tag{5.4}$$

where v_s is a velocity of s-electrons.

At the third step, we define the required average frequency of s-d electron collisions $\bar{\nu}_{sd}(T_e)$ using the Drude relation. We do this using the calculated values $\kappa_{sd}(T_e)$ (5.4), the average squared velocity of s-electrons, and their heat capacity per unit volume $C_s(T_e)$

$$\bar{\nu}_{sd}(T_e) = (1/3)\,C_s(T_e)\,\bar{v}_s^2/\kappa_{sd}(T_e). \tag{5.5}$$

The function (5.5) is shown in Fig. 5b.

It is significant to emphasize the importance of calculations of the e-e processes. Recent methods of description of conductivity based on the DFT packages and Kubo-Greenwood formula [27] do not include the e-e kinetic processes.

6. TWO-TEMPERATURE THERMAL CONDUCTION INCLUDING E-I AND E-E SCATTERING

Above we have calculated the average frequencies of s-s and s-d processes (the s-s procedure is taken from [24]). The results of calculation are shown in Fig. 5b. Addition of frequencies $\nu_{si}+\bar{\nu}_{ss}+\bar{\nu}_{sd}$ (4.1) is equivalent to the sequential addition of resistances in the electrical circuit. Which frequency in the sum $\nu(T_e,T_i) = \nu_{si}(T_i)+\nu_{se}(T_e)$ dominates, depends on the temperatures T_e and T_i. There is a range of temperatures T_e and T_i where the s-e scattering dominates. The dependence $\nu(T_e,T_i)$ is shown in Fig. 6a.

This situation with significant s-e scattering (not typical for normal conditions) is important for fast laser heating considered here. Indeed, during the very initial stage of propagation of electron heat wave electrons are hot while ions are cold. In this case ions keep their crystal order, and the e-i scattering is rather unimportant. While electrons partially lose their degeneracy and collide frequently. In this situation the s-e collisions limit the 2T heat conduction κ in cold crystal and hence limit the propagation velocity of a thermal wave.

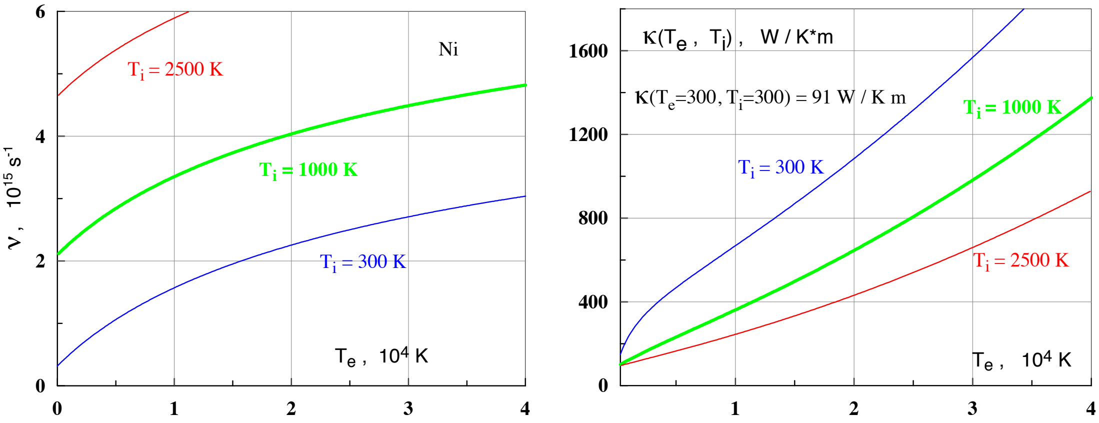

FIGURE 6. (a) (Color online) Total scattering frequency $\nu(T_e,T_i) = \nu_{si}(T_i) + \nu_{se}(T_e)$ as function of temperatures T_e and T_i. Partial frequencies ν_{si} and ν_{se} are shown in Figs. 4b and 5b, respectively. We see that at $T_i \sim 1$ kK the contributions of the s-i and s-e processes are comparable at $T_e \sim 20$ kK. (b) (Color online) Two-temperature thermal conductivity $\kappa(T_e,T_i)$. Increase of ion temperature T_i increases s-i collision rate and therefore decreases κ.

Thermal conductivity κ in two-temperature case is shown in Fig. 6b. At the temperatures $T_i = 0.3$ kK, $T_e = 20$ kK the conductivity κ is the order of magnitude higher than the room temperature value (1100 W/K·m versus 91). If we do not include s-e scattering then the value $\kappa(T_e = 20\,\text{kK}, T_i = 0.3\,\text{kK})$ will be seven times higher than the value $\kappa(T_e = 20\,\text{kK}, T_i = 0.3\,\text{kK}) = 1100$ W/K·m shown in Fig. 6b. This example emphasizes importance of the e-e processes which significantly decrease thermal diffusivity and thickness d_T of a heated layer. Consequently, the e-e processes influence the value of ablation threshold and depth of a crater at the threshold, see Fig. 1a.

7. TWO-TEMPERATURE HYDRODYNAMICS

2T-HD code integrates kinematical and dynamical equations together with mass conservation

$$\frac{\partial x(x^0,t)}{\partial t} = u(x^0,t), \quad \rho(x^0,t)\frac{\partial x(x^0,t)}{\partial x^0} = \rho^0, \quad \rho^0\frac{\partial u}{\partial t} = -\frac{\partial p(x^0,t)}{\partial x^0}, \tag{7.1}$$

and heat balances for electron and ion subsystems

$$\rho^0\frac{\partial(E_e/\rho)}{\partial t} = -\frac{\partial q}{\partial x^0} - \frac{\rho^0}{\rho}\alpha\cdot(T_e - T_i) + \frac{\rho^0}{\rho}Q - p_e\frac{\partial u}{\partial x^0}, \quad q = -\frac{\rho\kappa}{\rho^0}\frac{\partial T_e}{\partial x^0} \tag{7.2}$$

$$\rho^0\frac{\partial(E_i/\rho)}{\partial t} = \frac{\rho^0}{\rho}\alpha\cdot(T_e - T_i) - p_i\frac{\partial u}{\partial x^0}. \tag{7.3}$$

The unknown variables in (7.1)-(7.3) are functions of (x^0,t), where $x^0 = x(x^0, t = -\infty)$ is Lagrangian coordinate, $x(x^0,t)$ is a trajectory of a Lagrangian point x^0, x is direction

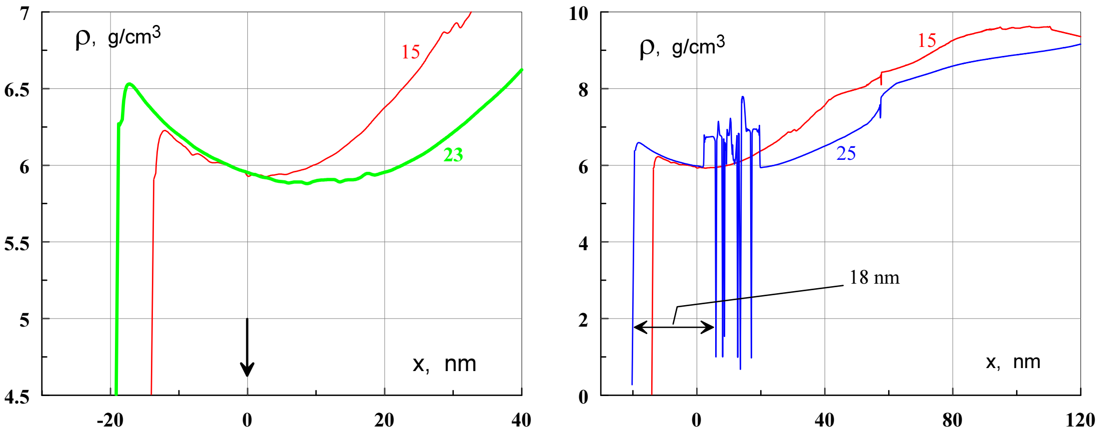

FIGURE 7. (a) (Color online) Instant density profiles before and shortly after beginning of nucleation. The digits "15" and "23" mean the time instants $t = 15$ ps and $t = 23$ ps. The arrow marks initial position of the vacuum-Ni boundary $x(x^0 = 0, t = -\infty)$. The narrow dip appears shortly after nucleation. There are two narrow layers, where density increases, at the left and the right sides of the dip. Density increases in these layers since negative pressure of stretched Ni rises to zero inside the layers due to termination of stretching. (b) (Color online) Thickness $x^0_{crat} = 18$ nm of the spallation layer on Lagrangian length x^0 and absorbed fluence $F_{abs} = 150$ mJ/cm^2 agree with experimental threshold crater depth x_{abl} (1.3) and F_{abl} (1.2) given in Section 1 and Fig. 1a. The spallation layer is denoted as the label "18 nm". The digits "15" and "25" mean the time instants $t = 15$ ps and $t = 25$ ps. Comparing the instants 23 and 25 ps in the left and right panels, we see that situation in the nucleation zone changes fast near the instant of beginning of nucleation.

of motion, p_e, p_i and p are partial and total pressures, E_e, E_i are partial energies per unit of volume, see Sections 2 and 3 above, Q is a source of energy due to absorption of a laser pulse. Coefficient κ in equation (7.2) for heat flux q has been described in Section 6.

Results of typical 2T-HD simulation is presented in Figs. 7 (a, b). Laser energy $F_{abs} = 150$ mJ/cm^2 is absorbed at a vacuum-Nickel boundary of a thick target. Maximum electron temperature ≈ 22 kK is achieved at the end of the laser pulse. Duration of the pulse is 80 fs as in the experiments described in Section 1. Electron-ion temperature equilibration processes proceeds $t_{eq} \approx 7-9$ ps. Electron pressure p_e is ≈ 40 GPa at the end of the pulse. Further electron contribution into total pressure $p = p_e + p_i$ decreases and at $t > t_{eq}$ we have $p_i \approx p$.

Laser action onto bulk Nickel has been considered in the paper [3]. This was a MD approach. Larger values of electron heat capacity $1065 T_e$ J$\cdot$K$^{-1} \cdot m^{-3}$ and electron heat conductivity $\kappa_{rt} T_e/T_i$, than presented above, have been used in [3]; here $\kappa_{rt} = \kappa(\rho_0, T_e = 300\,\mathrm{K}, T_i = 300\,\mathrm{K}) = 91$ W$\cdot K^{-1} \cdot m^{-1}$ is a heat conduction coefficient at room temperature. Increases of heat capacity and heat conductivity compensate each other when we calculate the 2T thermal diffusivity. This diffusivity, together with duration of 2T stage, defines thickness of heated layer d_T. Depth of a crater at an ablation threshold x_{abl}, see (1.3), is of the order of thickness of the heated layer d_T. Therefore the heat diffusivity influences ablation threshold F_{abl} (1.2): larger x_{abl} corresponds to larger F_{abl} (if material strength is the same). In [3] the values x_{abl}, F_{abl} are 25-30% higher than results of this paper. Duration of a laser pulse τ_L in [3] is 1 ps. This duration is longer

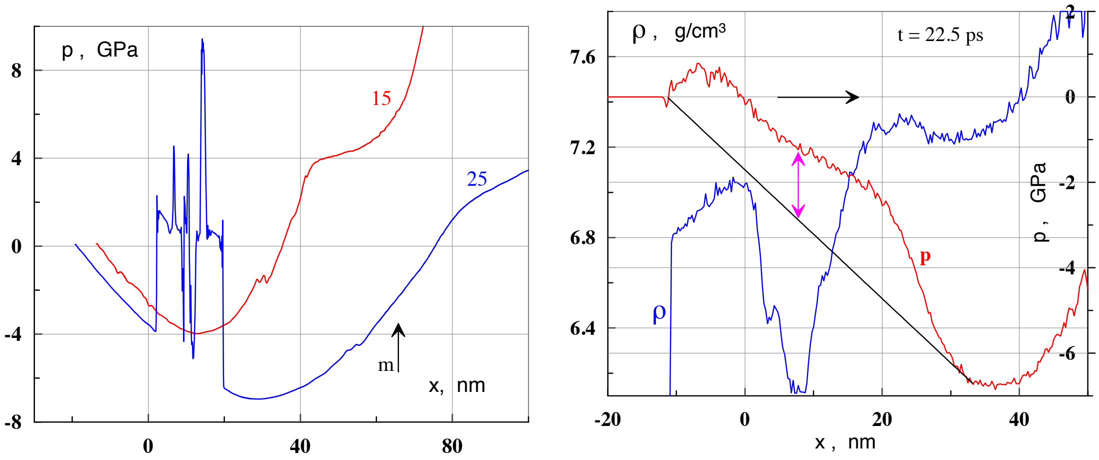

FIGURE 8. (a) (Color online) 2T-HD. Instant pressure profiles before and after nucleation. It is clear that deepening of the pressure well $p < 0$ takes place due to expansion caused by motion of the vacuum-metal boundary to the left side. The boundary is at the left side in the point where $p = 0$. After nucleation two shocks begin to propagate from the nucleation layer. The shocks rise pressure from negative values of pressure ahead the shocks. The digits "15" and "25" mean the time instants $t = 15$ ps and $t = 25$ ps. The arrow "m" corresponds to position of a melting front. (b) (Color online) Molecular dynamics (MD) simulation with $F_{abs} = 150$ mJ/cm^2. In MD simulation the pressure in the nucleation region more slowly rises after nucleation than in 2T-HD since in MD the foam appears [9]. The foam continues to resist to stretching. While in 2T-HD the material ceases to resist after few integration time steps after nucleation.

than considered above (80 fs). If duration τ_L is smaller than temperature equilibration time $t_{eq} \sim 7$ ps then a specific value of pulse duration τ_L weakly affects the ablation threshold x_{abl}, F_{abl} (F_{abl} increases with increase of τ_L).

Profiles of tensile stress are shown in Fig. 8 (a, b). Stretching of Nickel by tensile stress leads to nucleation. Nucleation takes place if absorbed fluence F_{abs} overcomes an ablation threshold F_{abl}. Experimental value for the threshold F_{abl} is given by (1.2). 2T-HD simulation shown in Figs. 7 and 8a corresponds to the case when F_{abs} is slightly above the threshold F_{abl}. Therefore nucleation takes place in few separated positions at the x axis. One shock running from nucleation position rises pressure from $p < 0$ to $p \approx 0$. Collision of shocks running from two neighboring positions doubles the pressure increment. Therefore there are places with $p > 0$ inside the layers where material "knows" that nucleation has occurred, see Fig. 8a.

In 2T-HD we use picture of thermal fluctuations to define place and instant where nucleation begins. Nucleation begins if the time τ_{nucl} for creation of a viable void becomes smaller than the expansion time τ_{expan} [5]. The time τ_{expan} is the least from the two times. One is the time during which the Lagrangian particle is under tensile stress. Another time is the inverse deformation rate $V/\dot{V}$. Nucleation time [28] is

$$\tau_{nucl} = \frac{|p|\,\eta}{V_{nucl}(\rho/m_{at})^2\sigma^{3/2}\sqrt{k_B T_i}}\exp\frac{W}{k_B T_i}, \qquad W = \frac{16\pi}{3}\frac{\sigma^3}{p^2}.$$

Here η is dynamical viscosity, $\sigma = \sigma_0(1 - T_i/T_c)^{1.25}$ is surface tension, T_c is critical temperature. Volume V_{nucl} is equal to causally linked neighborhood

$V_{nucl} = (4\pi/3)(c_s \tau_{nucl})^3$ of the nucleation point. In 2T-HD the pressure in nucleation point after nucleation is equal to zero.

Temperature in the nucleation points shown in Figs. 7 and 8 is 2.5 kK. Before nucleation Nickel is significantly stretched. Its equilibrium density at this temperature is 7.3 g/cm^3, see Fig. 3a. The arrow "m" in Fig. 8a marks the right end of molten Nickel.

CONCLUSIONS

Experimental results relating to single shot action on a target are presented. They include measurements of absorbed energy and final topology of irradiated laser spot. Consistent approach, based on calculations of electron conductivity in 2T state, allows us to adjust the data and simulations.

ACKNOWLEDGMENTS

This work was supported by the ONR, NRL and NSF. Calculations were performed using NSF TeraGrid facilities, the USF Research Computing Cluster, and computational facilities of the Materials Simulation Laboratory at USF Physics Department. This work was supported by the Russian Foundation for Basic Research (project no. 10-08-92661-NNF-a) and the US National Science Foundation (grant no. DMR-1008676) in the framework of the joint project "Materials World Network." The work of S.I.A., N.A.I., M.B.A., and S.I.Anisimov was supported by the Russian Foundation for Basic Research (project no. 10-02-00434-a). The work of S.I.A., and M.B.A. was supported by the Ministry of Education and Science of the Russian Federation (state contract no. 14.740.11.0064).

REFERENCES

1. Anisimov, S. I., Kapeliovich, B. L., and Perel'man, T. L., *Sov. Phys. JETP*, **39**, 375–377 (1974).
2. Inogamov, N. A., Zhakhovskii, V. V., Ashitkov, S. I. et al., *Contrib. Plasma Phys.*, **51**, 367–374 (2011).
3. Zhigilei, L. V., Lin, Zh., and Ivanov, D. S., *J. Phys. Chem. C*, **113,** 11892 (2009).
4. Lewis, L. J. and Perez, D., Chapter 2, in book: K. Sugioka et al. (eds.), *Laser Precision Microfabrication*, Springer Ser. Mater. Sci., Vol. 135, DOI 10.1007/978-3-642-10523-4, Springer-Verlag Berlin Heidelberg (2010).
5. Povarnitsyn, M. E., Itina, T. E., Sentis, M. et al., *Phys. Rev. B*, **75,** 235414 (2007).
6. Lin, Zh., Zhigilei, L. V., Celli, V., *Phys. Rev. B*, **77,** 075133 (2008).
7. Anisimov, S. I., Inogamov, N. A., Petrov, Yu. V. et al., *Appl. Phys. A* **92,** 939–943 (2008); *ibid* **92,** 797–801 (2008).
8. Leveugle, E., Ivanov, D. S., Zhigilei, L. V., *Appl. Phys. A*, **79,** 1643–1655 (2004).
9. Demaske, B. J., Zhakhovsky, V. V., Inogamov, N. A., Oleynik, I. I., *Phys. Rev. B*, **82,** 064113 (2010).
10. Gill-Comeau, M., Lewis, L. J., *Phys. Rev. B*, **84,** 224110 (2011).
11. Agranat, M. B., Andreev, N. E., Ashitkov, S. I., Veisman, M. E., Levashov, P. R., Ovchinnikov, A. V., Sitnikov, D. S., Fortov, V. E., Khishchenko, K. V., *JETP Lett.*, **85,** 271–276 (2007).
12. Inogamov, N. A., Zhakhovskii, V. V., Ashitkov, S. I., Petrov, Yu. V., Agranat, M. B., Anisimov, S. I., Nishihara, K., Fortov, V. E., *JETP*, **107**(1), 1–19 (2008).

13. Agranat, M. B., Ashitkov, S. I., Ivanov, A. A., Konyashchenko, A. V., Ovchinnikov, A. V., V E Fortov, V. E., *Quantum Electronics*, **34**(6), 506-Ű508 (2004).
14. Zornberg, E. I., *Phys. Rev. B*, **1**(1), 244–263 (1970).
15. Wang, C. S., Callaway, J., *Phys. Rev. B*, **9**(11), 4897–4907 (1974).
16. The ABINIT code is a common project of the Universite Catholique de Louvain, Corning Incorporated, and other contributors (http://www.abinit.org).
17. http://www.vasp.at/
18. Kresse, G., Hafner, J., *Phys. Rev. B*, **47**, 558–561 (1993).
19. Delley, B., *J. Chem. Phys.* **92**, 508–518 (1990); Delley, B., *J. Chem. Phys.* **113**, 7756–7765 (2000). http://accelrys.com/
20. Alemany, M. M. G., Gallego, L. J., Gonzalez, D. J., *Phys. Rev. B*, **70**, 134206 (2004).
21. Khakshouri, S., Alfe, D., Duffy, D. M., *Phys. Rev. B*, **78**, 224304 (2008).
22. Starikov, S. V., Stegailov, V. V., Norman, G. E., Fortov, V. E., Ishino, M., Tanaka, M., Hasegawa, N., Nishikino, M., Ohba, T., and Kaihori, T., et al. *JETP Lett.*, **93**, Number 11, 642–647 (2011).
23. Shock wave database: http://teos.ficp.ac.ru/rusbank/.
24. Inogamov, N. A., Petrov, Yu. V., *JETP*, **110**, Number 3, 446–468 (2010).
25. Wilthan, B., Cagran, C., Pottlacher, G., *Intern. J. Thermophys.*, **25,** Number 5, 1519–1534 (2004).
26. http://riodb.ibase.aist.go.jp/TPDB/AJAX/index.aspx?Search=nickel%2C+Ni
27. Recoules, V., Crocombette J.-P., *Phys. Rev. B*, **72,** 104202 (2005).
28. Deryagin, B.V., *Zhurnal Teor. Eksp. Fiziki*, **65,** No. 6, 2261 (1973).